

Hot deformation behavior of CrMnFeCoNi equiatomic FCC High Entropy Alloy

Eleti Rajeshwar Reddy

A Dissertation Submitted to
Indian Institute of Technology Hyderabad
In Partial Fulfillment of the Requirements for
The Degree of Master of Technology



भारतीय प्रौद्योगिकी संस्थान हैदराबाद
Indian Institute of Technology Hyderabad

Department of Materials Science and Metallurgical Engineering

JUNE, 2015

Declaration

I declare that this written submission represents my ideas in my own words, and where others' ideas or words have been included, I have adequately cited and referenced the original sources. I also declare that I have adhered to all principles of academic honesty and integrity and have not misrepresented or fabricated or falsified any idea/data/fact/source in my submission. I understand that any violation of the above will be a cause for disciplinary action by the Institute and can also evoke penal action from the sources that have thus not been properly cited, or from whom proper permission has not been taken when needed.



(Signature)

Eleti Rajeshwar Reddy

(- Student Name -)

MS13M1005

(Roll No)

Approval Sheet

This thesis entitled "Hot deformation behavior of CoCrFeMnNi equiatomic FCC High Entropy Alloy" by Eleti Rajeshwar Reddy is approved for the degree of Master of Technology from IIT Hyderabad.



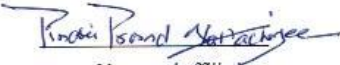
-Name and affiliation-

Examiner


8.0.6-2013

-Name and affiliation-

Ehsan B. Parizadeh
Examiner



-Name and affiliation-

Adviser

-Name and affiliation-

Co-Adviser



-Name and affiliation-

Viswanath R. Chintalapudi
MAE Chairman

Acknowledgements

I would like to express my sincere gratitude to my thesis supervisor **Dr. Pinaki Prasad Bhattacharjee** (Associate Professor and Head of the Department) for his valuable suggestions during this research work. I would also like to thank **Professor Nobuhiro TSUJI** (Dept. of Materials Science and Engineering, Kyoto University, JAPAN) who permitted and encouraged to carry out the hot compression experiments in his lab. I would like extend my acknowledgements to Mr. Lijia Zhao and Mr. Tilak Bhattacharjee (Kyoto University, JAPAN) for their help to carry out the hot compression tests. My sincere appreciations to Mr. Dan Sathiaraj (PhD) who helped me in handling various equipment. I thank all my friends and fellow research scholars who dedicated their time in helping me.

Dedicated to

All the Special Forces and their families.

Abstract

The evolution of microstructure and texture during hot deformation was investigated in an equiatomic multicomponent CoCrFeMnNi alloy. For this purpose the alloy was obtained in the cast form and thermos-mechanically processed to obtain a wrought microstructure with average grain size of $\sim 28 \mu\text{m}$. Hot compression samples were subsequently extracted from this alloy. The hot compression tests were carried out at temperatures ranging from 700°C to 1000°C and strain rates varying from $0.001/\text{s}$ to $1/\text{s}$. The flow curves were analyzed for understanding the deformation behavior. The microstructure and texture evolution was investigated using electron backscatter diffraction system.

The analysis of the flow curve yielded an apparent activation energy for deformation $\sim 350 \text{ kJ mol}^{-1}$. This was found close to the activation energy for the diffusion of the slowest diffusing element Ni. The microstructural analysis indicated that the dynamically recrystallized grains nucleated along the shear bands and prior grain boundaries resulting in the formation of typical necklace structure. Significant grain size refinement was achieved due to dynamic recrystallization. The grain size of dynamically recrystallized regions also showed strong dependence on the Zener-Holloman parameter.

The texture of deformed and dynamically recrystallized grains were found to be similar but rather weak. This feature could be attributed to the nucleation of dynamically recrystallized without any preferential orientation selection.

Nomenclature

HEA- High Entropy Alloy

DRX- Dynamic Recrystallization

CA- Compression Axis

FCC- Face Centered Cube

BCC- Body Centered Cube

ECAP- Equi-Channel Angular Pressing

HPT- High Pressure Torsion

ARB- Accumulative Roll Bonding

XRD- X Ray Diffraction

SEM- Scanning Electron Microscope

EBSD- Electron Backscatter Diffraction

GAM- Grain Average Misorientation

Z- Zener Hollomon parameter

σ - True Stress (MPa)

ε - True Strain

Q- Activation Energy (kJmol^{-1})

R- Universal Gas constant ($\text{JK}^{-1}\text{mol}^{-1}$)

IPF- Inverse Pole Figure

HAGB- High Angle Grain Boundary

LAGB- Low Angle Grain Boundary

Contents

Declaration	ii
Approval Sheet	iii
Acknowledgements	iv
Abstract	vi
Nomenclature	vii
1 Introduction	1
1.1 High Entropy Alloys	
1.2 Objectives of present study	2
2 Literature Review	
2.1 Development of HEAs	3
2.2 Thermo-Mechanical processing of HEAs	4
2.3 Objective and Significance of present study	5
3 Experimental Procedure	
3.1 Starting Material	7
3.2 Processing	7
3.2.1 Preparation of sample for hot compression	7
3.2.2 Hot Compression	8
3.3 Microstructural Observations	10
4 Results	
4.1 Starting Material	12
4.2 Flow Curves	14
4.3 Calculation of hot deformation parameters	16
4.4 Evolution of Microstructure and Texture	25
5 Discussion	
5.1 Flow curve and Hot deformation behavior	33
5.2 Evolution of Microstructure and Texture	33
6 Summary and Conclusions	35
References	36

Chapter 1: Introduction

1.1 High entropy alloys

The classical alloy design concept for developing structural materials is essentially focused on using one principal element to which other alloying elements are purposefully added in suitable proportion for introducing or improving desired properties. Well known examples of these materials are different grades of steels (iron base), aluminum, nickel or copper base alloys. In contrast, high entropy alloys (HEAs) are recently developed multicomponent alloys having five or more elements in equiatomic or near equiatomic proportion. In spite of the presence of a large number of elements the HEAs surprisingly have simple FCC, FCC+BCC or BCC structures. It is hypothesized at the present state of knowledge that high configurational entropy associated with the mixing of a large number of elements stabilizes phases with simple crystal structures. The HEAs have generated tremendous research interest in recent times due to the possibility of developing many new alloy systems with unique properties. High entropy, sluggish diffusion, severe lattice distortion and cocktail effects are found to be the significant factors in affecting the structures and properties of HEAs.

The majority of the early investigations on HEAs has been carried out on as-cast alloys for understanding the phase stability. Although high hardness, wear and abrasion resistance have been observed in HEAs even in the as-cast conditions, it is expected that development of HEAs with ultrafine (average grain size $\leq 1 \mu\text{m}$) to nanostructure (average grain size $\leq 0.1 \mu\text{m}$) by appropriate thermo-mechanical processing route can greatly enhance the properties and widen the possible applications of these alloys.

The advent of different severe plastic deformation techniques, such as, equi channel angular pressing (ECAP), high pressure torsion (HPT) or accumulative roll bonding (ARB) has made it

possible to achieve ultrafine to nanocrystalline grain size in a wide variety of materials. Although these techniques remain scientifically intriguing, scaling up these techniques for continuous and bulk production remains a key challenge. In contrast, hot deformation of materials (i.e. plastic deformation of materials above the recrystallization temperature) which is a widely accepted and established technique for microstructure refinement can also result in achieving ultrafine grain size under suitable processing conditions. Therefore, from the point of view of applications of these alloys in of future structural applications of HEAs, hot-deformation approach for developing ultrafine HEAs appears to be more attractive than other SPD routes.

1.2 Objectives of the present study

The present work attempts to understand the hot deformation behavior of high entropy alloys (HEAs) with particular reference to microstructure and texture formation. Equiatomic CoCrFeMnNi with simple FCC structure is studied as the model alloy system. The hot deformation has been carried out by varying the processing parameters. Careful characterization at different length scales using X-ray Diffraction (XRD), Scanning Electron Microscopy-Electron Backscatter Diffraction (SEM-EBSD) techniques.

Chapter 2: Literature Review

2.1 Development of high entropy alloys

The classical alloy design concept for developing structural materials is essentially focused on using one principal element to which other alloying elements are added purposefully in suitable amount for introducing or improving desired properties. Well known examples of these materials are different grades of steels (iron base), aluminum, nickel or copper base alloys. In contrast, recently a new alloy design concept has been introduced for developing novel structural materials which are multicomponent alloys having equal to or more than five elements with almost equal proportion [1]. These materials have assumed the generic name high entropy alloys (HEAs) due to the very high configurational entropy associated with the mixing of a large number of elements. These alloys, although, contain a large number of principal elements, but the structure remains essentially simple, many times FCC or BCC [2]. The research on HEAs has gained considerable attention in recent years and many interesting and unique properties of these materials have been reported [3-9]. The unique properties of the HEAs are attributed to the core effect of multicomponent solid solution formation, namely distorted lattice structure [3, 4], cocktail effect [3, 4], sluggish diffusion [3, 4, 10] and formation of nanoscale deformation twins [5, 11]. The potential of these alloys in terms for various engineering applications such as wear and abrasion resistant material [12, 13] have already been recognized. Many of the early investigations on HEAs are carried out on as-cast materials. However, it is well known that thermo-mechanical processing can greatly refine the microstructure and enhance the properties of materials. As a result thermo-mechanical processing remains a topic of much interest for HEAs. It may be noted that the advent of different severe plastic deformation (SPD) processing techniques such as Equi Channel Angular Pressing (ECAP) [14], High Pressure Torsion (HPT)

[15] or Accumulative Roll Bonding (ARB) [16] has made it possible to achieve ultrafine to nanostructure in a wide range of materials. However, these processing routes are not amenable to continuous production at their present state of development. Therefore, microstructural refinement through conventional thermo-mechanical processing routes remains particularly important for HEAs.

2.2 Thermo-mechanical processing of HEAs

Thermo-mechanical processing involving heavy deformation and annealing has been investigated on different HEAs [17-22]. A number of studies have used the equiatomic FCC CoCrFeMnNi as a model system for this purpose. It has been recently clarified by the research group at IIT Hyderabad that large cold-rolling reduction ($\geq 90\%$ reduction in thickness) followed by suitable annealing treatments can yield ultrafine microstructure (Fig.2.1) [23, 24]. The evolution of such ultrafine microstructure has been attributed to nucleation inside homogeneously deformed matrix, but restricted grain growth due to sluggish diffusion. The HEA also shows exceptional resistance against grain growth with rather high activation energy for grain growth [25]. It is well-known that significant microstructural refinement can also be achieved in a wide range of materials by suitable hot-deformation processing. For low SFE alloys microstructural development during hot deformation involve dynamic recrystallization leading to the formation of a necklace type structure (Fig.2.2). The hot deformation behavior of HEAs has been investigated only to a very limited extent. Although the hot deformation behavior of the equiatomic FCC CoCrFeMnNi has been reported very recently, detailed microstructural development has not been reported [26].

2.3. Objective and significance of the present study

It is evident that low SFE of the CoCrFeMnNi and sluggish diffusion in this system make this alloy quite suitable for investigating the possibility of achieving ultrafine microstructure using conventional hot deformation based thermo-mechanical processing approach. This clearly requires appropriate understanding of the flow behavior and microstructure development during hot deformation, which essentially constitute the major focus of present research.

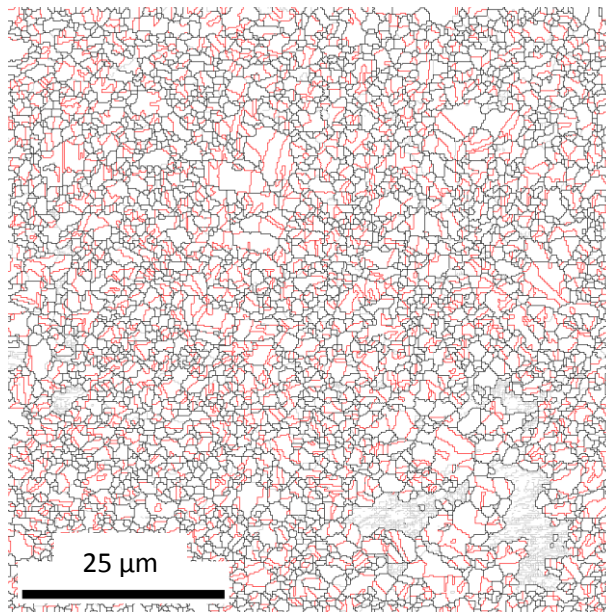


Fig.2.1: Grain boundary map of equiatomic CoCrFeMnNi after 95% cold-rolling at annealing at 700°C. The black, gray and red lines are the high angle boundaries and twin boundaries, respectively. The average recrystallized grain size is $\sim 1\mu\text{m}$ [23].

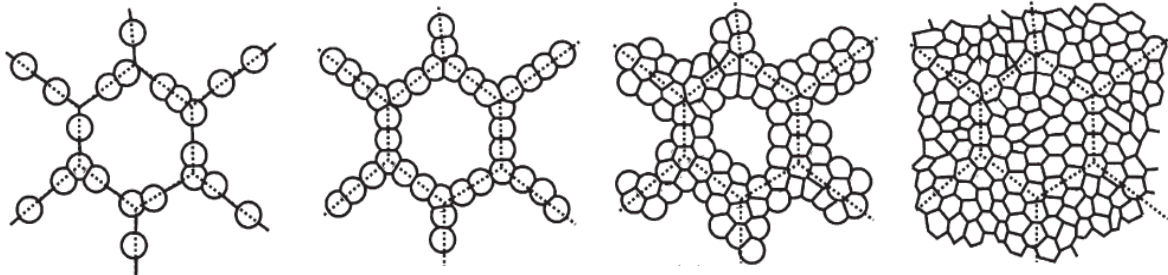


Fig. 2.2: Schematic of the process of microstructural evolution during hot deformation [27].

Chapter 3: Experimental Procedure

3.1 Starting material

Equiatomic CoCrFeMnNi HEA was selected for the present investigation. The alloy was prepared using a well-developed vacuum arc melting route. Co and Ni were taken in the form of small cubes and balls respectively, while the others constituents in the form of chips for the melting purpose. The melt was re-melted for three times to improve the homogeneity. A Vacuum Arc Melting unit (Make: M/S Vacuum Techniques, Bengaluru, INDIA) was used for the melting and remelting purpose. The melt was cast into a pancake shape with dimensions of 20mm (thickness) * 80mm (diameter).

3.2 Processing

3.2.1 Preparation of the samples for hot compression

The as cast alloy was homogenized at 1100°C for 6 hours (h). The homogenized alloy was subsequently hot forged at 800°C to 30% reduction in thickness. Cylindrical compression samples having dimensions 8mm (diameter) x 14 mm (height) were extracted from the hot forged material using electro discharge machining (EDM). The procedure for obtaining the compression samples could be summarized in Fig.3.1.

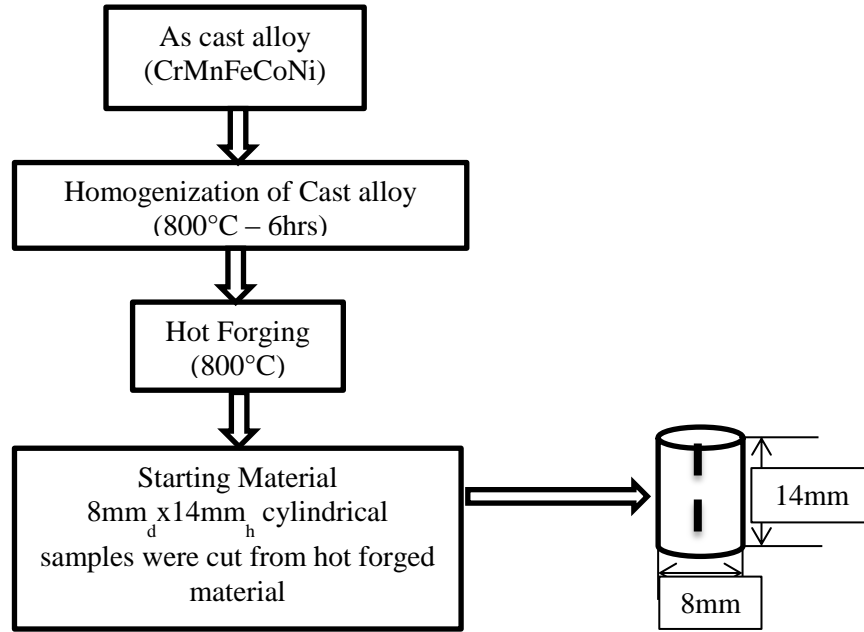


Fig. 3.1: Flow chart showing preparation of the samples for hot compression.

3.2.2 Hot compression

Uniaxial hot compression testing was carried out in a thermo-mechanical processing simulator (Model: Thermecmaster-Z, Make: Fuji Electronic Industrial Company Ltd., Japan) installed at Kyoto University, Japan using various temperatures and strain rates. Mica with glass powder was used as insulator and lubricant. A thermocouple was welded to the compression samples at the mid-height region for precise temperature measurement. The samples were isothermally held at 1000°C for 15 minutes and then cooled at the rate of 2°C/s to the deformation temperature. Nitrogen jet was used as the cooling medium.

Fig.3.2 shows a representative image of the deformation chamber. Deformation was carried at a wide range of varying from 700°C to 1000°C in an intervals of 100°C using the strain rates of 10^{-3} , 10^{-2} and 10^0 s^{-1} . Once, the deformation temperature was attained, holding time of 10s was given for achieving homogeneity of temperature. For all the deformation conditions mentioned, a uniaxial compressive deformation was carried out to 60% reduction in height with an equivalent true strain of $\epsilon = 0.916$. As soon as the deformation was completed, the samples were quenched using the flowing N_2 jet. The experimental procedure and various conditions of the hot-compression testing could be summarized in Fig.3.3.

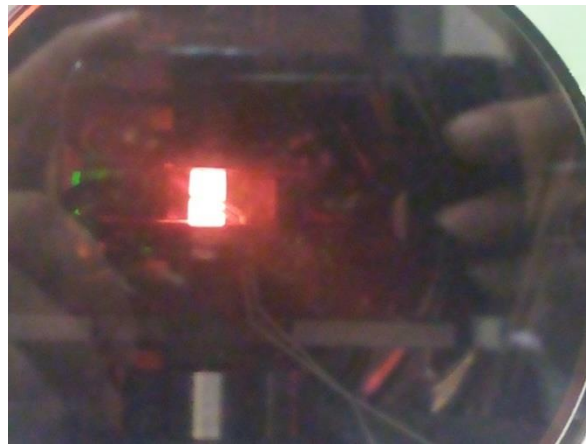


Fig.3.2: Deformation chamber of the thermo-mechanical processing simulator showing the sample in the red hot state just before the compression.

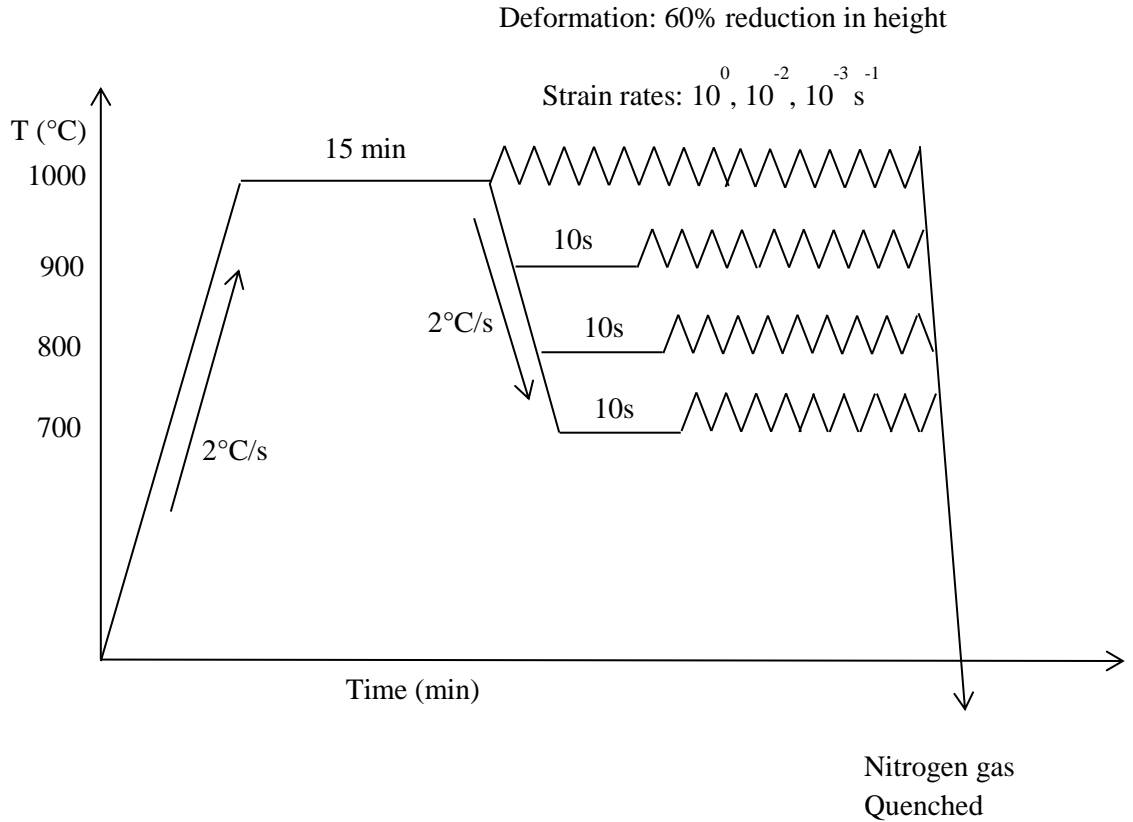


Fig.3.3: Experimental procedure and various conditions of the hot-compression testing.

3.3 Microstructural observations

The microstructure and texture of the hot compressed samples were characterized by Electron Back Scatter Diffraction (EBSD). For EBSD investigation, the hot-compressed samples were sectioned vertically through the center along the compression direction (Fig.3.4). The samples were carefully mechanically polished prior to electropolishing. The Electrolyte used for the electropolishing consisted of 10% perchloric acid and 90% methanol. The electropolishing was carried out at -5°C using a constant voltage of 15V applied for 15s.

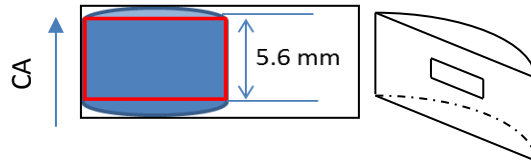


Fig.3.4: Schematic of the sample sectioning procedure for the EBSD measurements (CA = compression axis).

An EBSD system (Oxford Instruments, UK) attached to a Field Emission Scanning Gun type Scanning Electron Microscope (FEG-SEM, Make: Carl Zeiss, Germany, Model: SUPRA 40) was used in the present work. The EBSD scans were all obtained very close to center shown by enclosed square in Fig.4. A scan step size of $0.20\ \mu\text{m}$ was used for all the scans. The AzTec HKL software (Oxford Instruments, UK) was used for the data acquisition. The scan data was exported in the .ctf format for analysis using the TSL-OIMTM software (EDAX Inc., USA) for analysis purpose. The Inverse pole figures (IPFs) were calculated using the series expansion method with series rank 22.

The current study focuses mainly on the evolution of microstructure and texture in dynamically recrystallized (DRX) regions. In order to separate the DRX regions, a proper set of criteria was felt necessary. Kernel average based misorientation approach which has been used for this purpose by various authors was also adopted in this work. In the present study, KAM based approach was also used. The KAM was calculated up to 10 nearest neighbors using a cut-off angle of 5° . The recrystallized regions were defined as those satisfying the criteria of $\text{KAM} \leq 0.5^\circ$.

Chapter 4: Results and Discussion

4.1 Starting Material

Fig.3.3 suggests that the material which was annealed at 1000°C for 15 minutes can be considered as the starting material for the subsequent hot compression. The microstructure of starting materials is shown in Fig.4.1. This microstructure is obtained by quenching the material after annealing at 1000°C for 15 minutes. The Y axis of the map is parallel to the compression axis (CA). The average grains size of the starting recrystallized material is ~ 25 μm . The twins are not considered as separate grains for the calculation of grain size. The grain size distribution of the starting materials is shown in Fig.4.1(b) where presence of few large grains may be evident. The starting texture appear to be quite weak (Fig.4.1(c)).

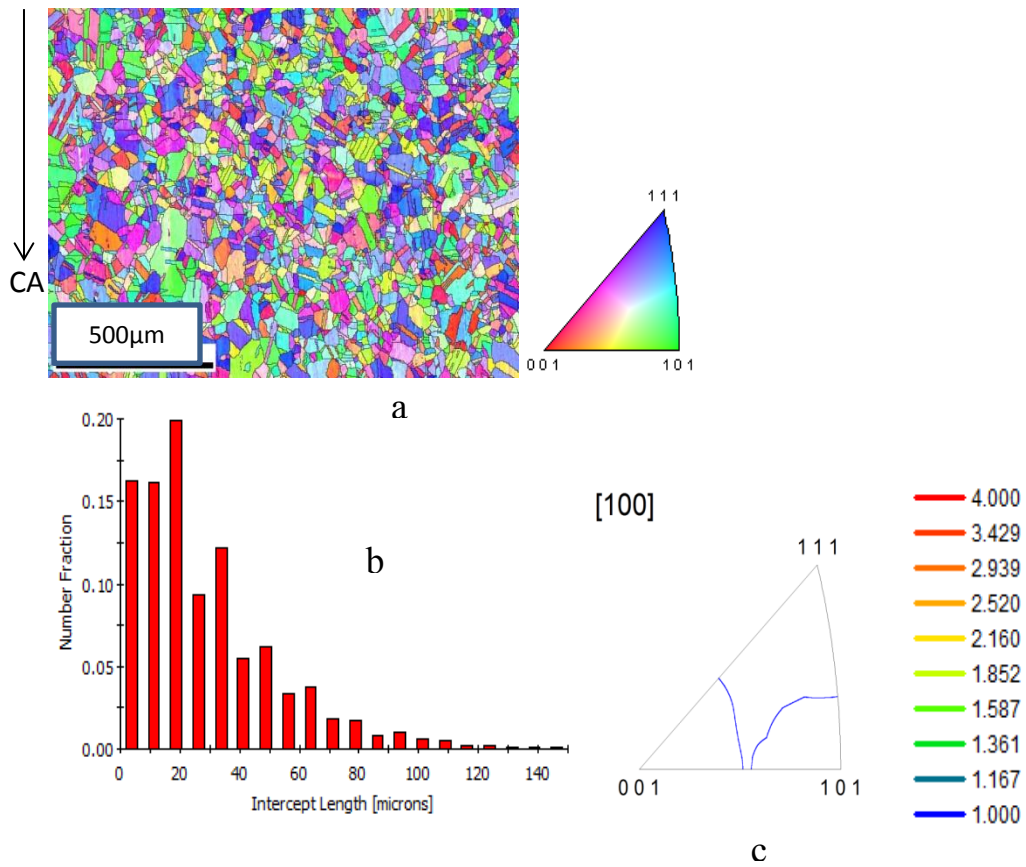


Fig.4.1: (a) Microstructure and (b) grain size distribution and (c) IPF plot (reference direction is the CA direction parallel to the Y axis of the map shown in Fig.4.1(a)) showing texture of the starting material i.e. obtained after annealing at 1000°C for 15 minutes.

4.2 Flow curves

Fig.4.2 shows flow curves for constant strain rate and different deformation temperatures. For any given strain rate, the flow stress is decreased with an increase in the deformation temperature. This is equivalent to saying that with decreasing Zener-Hollomon parameter ($Z = \dot{\epsilon} \exp(\frac{Q}{RT})$), the flow stress is reduced. This is indicative of the occurrence of dynamic recrystallization (DRX). This behavior is clearly summarized in Fig.4.3 which shows that the maximum peak stress decreases consistently with decreasing Z (i.e. with decreasing strain rate for a constant temperature or increasing temperature for a constant strain rate). However, the flow curves in Fig.4.2 indicate that even when the DRX is expected, the difference between the peak stress and steady state stress is rather small.

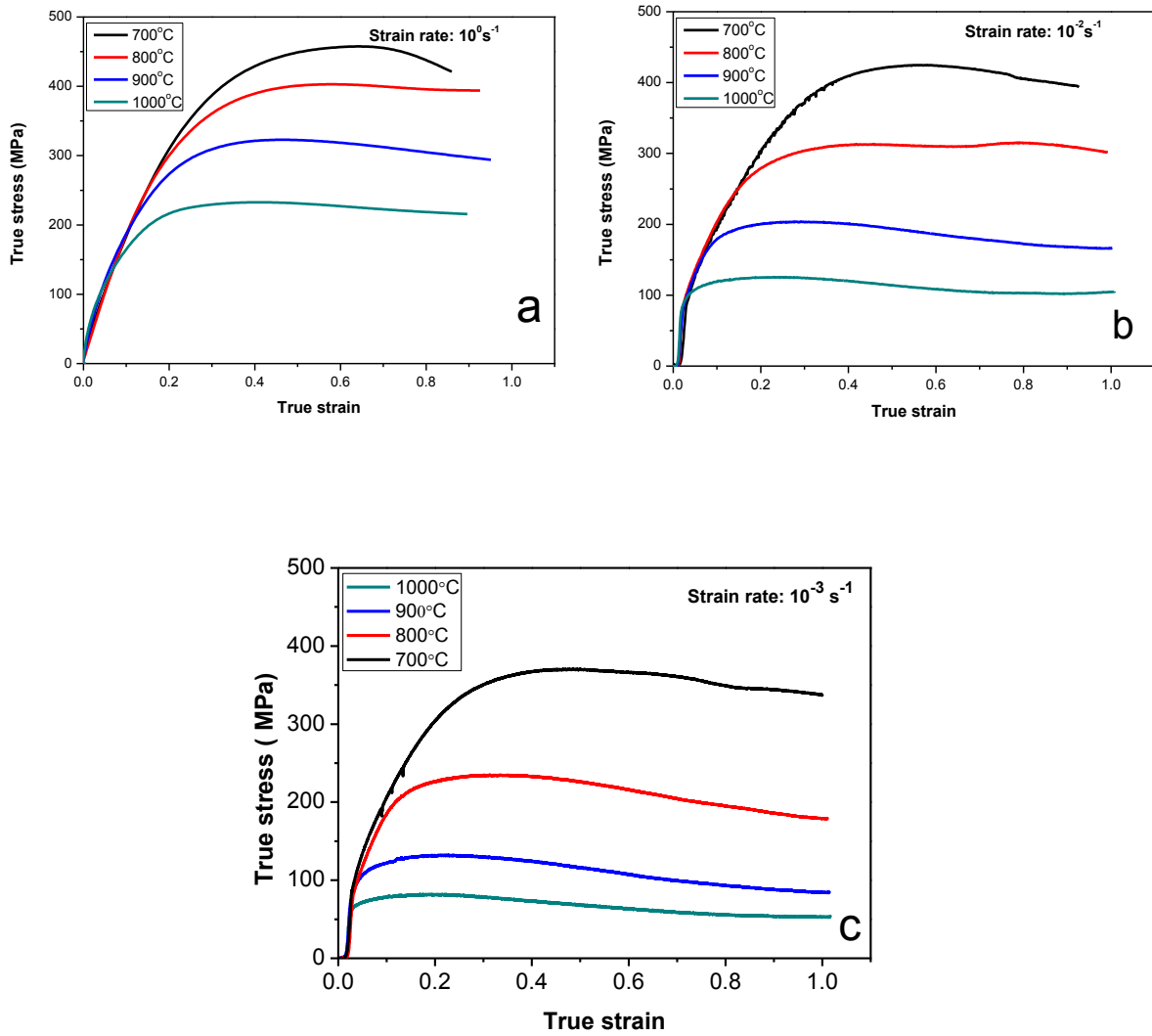


Fig.4.3: Flow curves at strain rates of (a) 10^0s^{-1} , (b) 10^{-2}s^{-1} (c) 10^{-3}s^{-1} and various deformation temperatures.

4.3 Calculation of hot deformation parameters:

The flow stress (σ) is affected by deformation temperature (T), strain rate ($\dot{\epsilon}$) and strain during hot deformation. The interdependence of these parameters can be expressed by using appropriate constitutive equations. The Arrhenius type of equation is employed for expressing the relationship between $\dot{\epsilon}$, T and σ while the Zener-Holloman parameter [28] is used to correlate T and $\dot{\epsilon}$. The two relevant equation are given by:

$$Z = \dot{\epsilon} \exp\left(\frac{Q}{RT}\right) \quad \text{Eq. 4.1}$$

And

$$\dot{\epsilon} = Af(\sigma)\exp\left(-\frac{Q}{RT}\right) \quad \text{Eq. 4.2}$$

$f(\sigma)$ is a function which varies depending up on the stress level as summarized below:

$$\begin{aligned} f(\sigma) &= \sigma^{n_1} \text{ if } \alpha\sigma \leq 0.8 \\ &= \exp(\beta\sigma) \text{ if } \alpha\sigma \geq 1.2 \\ &= [\sinh(\alpha\sigma)]^n \text{ for all } \alpha \end{aligned} \quad \text{Eq. 4.3}$$

Q: activation energy of deformation (Jmol^{-1}), R: universal gas constant ($8.314 \text{ Jmol}^{-1}\text{K}^{-1}$), T: deformation temperature, σ : Flow stress (MPa), $\dot{\epsilon}$: strain rate (s^{-1}). A , α , β ($=\alpha n_1$), n and n_1 are constants.

The true stress-strain curves can be used to determine the constants. Substituting the Eq.4.3 in Eq.4.2,

$$\dot{\epsilon} = B\sigma^{n_1} \quad \text{Eq. 4.1}$$

and

$$\dot{\epsilon} = C\exp(\beta\sigma) \quad \text{Eq. 4.2}$$

In the above equations B and C are constants.

It can be easily derived from Eq.4.4 and Eq.4.5 that:

$$\ln \dot{\epsilon} = \ln B + n_1 \ln \sigma \quad \text{Eq. 4. 3}$$

$$\ln \dot{\epsilon} = \ln C + \beta \sigma \quad \text{Eq. 4. 4}$$

Therefore, the slope of the $\ln \dot{\epsilon}$ vs $\ln \sigma$ plot (Fig.4.2(a)) will supply the constant n_1 while the slope of $\ln \dot{\epsilon}$ vs σ (Fig.4.2(b)) will supply the constant β . It is clearly observed that slope of the straight lines in Fig.4.2 vary considerably with temperature. For instance the value of n_1 varies from 5.5 to 29. The estimated values of n_1 and β are 13 and 0.045. From these values α ($= \frac{\beta}{n_1}$) may be determined as 0.0035.

The hyperbolic sine form of $f(\sigma)$ ($= [\sinh(\alpha\sigma)]^n$) is suitable for both low and high stress levels. It may be easily shown that,

$$\dot{\epsilon} = A[\sinh(\alpha\sigma)]^n \exp\left(-\frac{Q}{RT}\right) \quad \text{Eq. 4. 8}$$

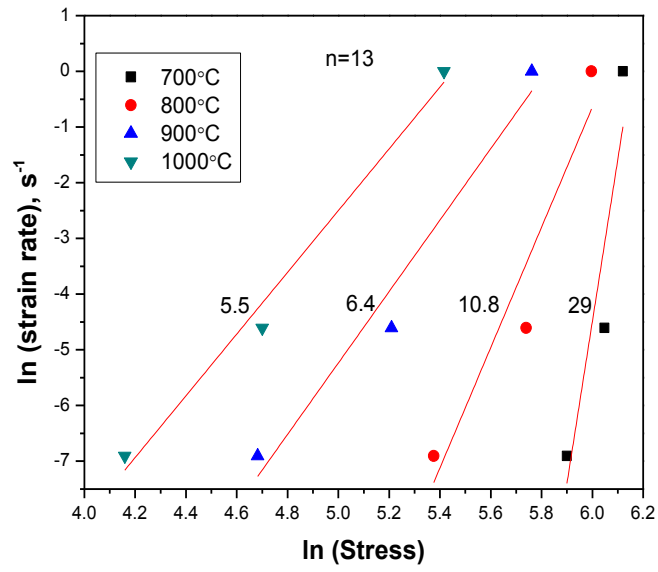
$$\ln[\sinh(\alpha\sigma)] = \frac{\ln(\dot{\epsilon})}{n} + \frac{Q}{nRT} - \frac{\ln A}{n} \quad \text{Eq. 4. 9}$$

The plot of $\ln[\sinh(\alpha\sigma)]$ vs $\ln \dot{\epsilon}$ for a particular temperature may be used to determine the value of n . A series of plots is shown in Fig.4.3(a). The average value of n determined from the plot is ~9.3.

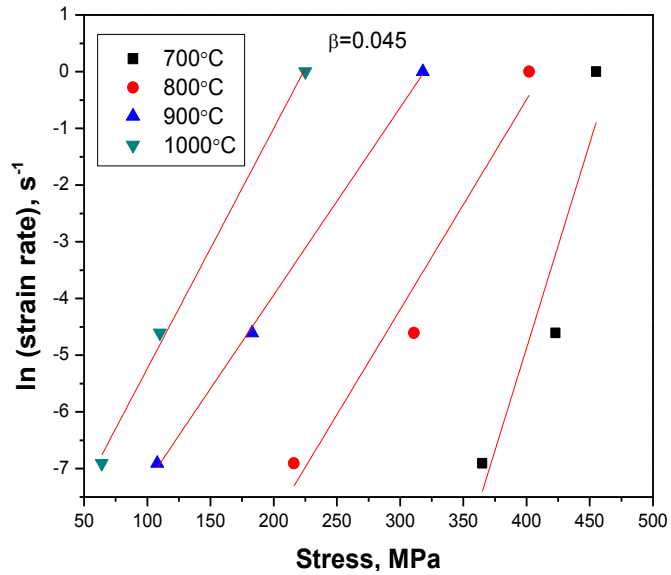
Differentiation of the Eq.4.8 shows that

$$Q = Rn \frac{d\{\ln[\sinh \alpha\sigma]\}}{d\left(\frac{1}{T}\right)} \quad \text{Eq. 4. 10}$$

Therefore, the slope of the curve $\ln[\sinh \alpha\sigma]$ vs $1/T$ is necessary for determining the activation energy (Fig.4.3(b)). Substituting the average slope in the Eq.4.10, the calculated activation energy at a strain of 0.6 was found to be 495 k J mol^{-1} . Similar analysis was carried out to estimate activation energy at strains 0.4, 0.6, 0.8 and 0.9 as well. The effect of strain on activation energy is shown in the Fig.4.4.

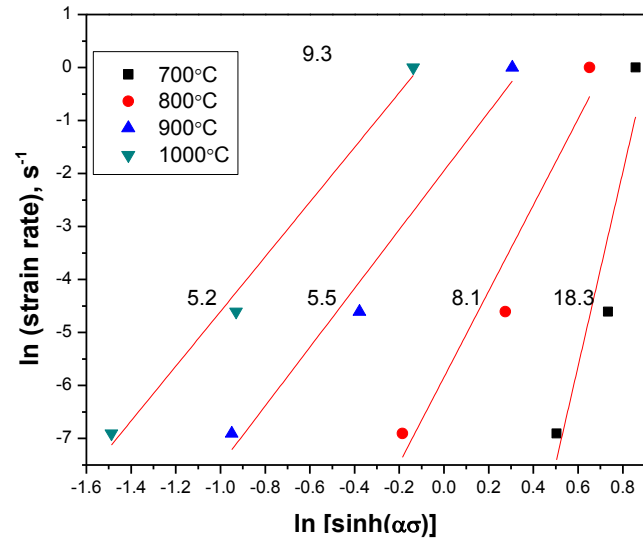


a

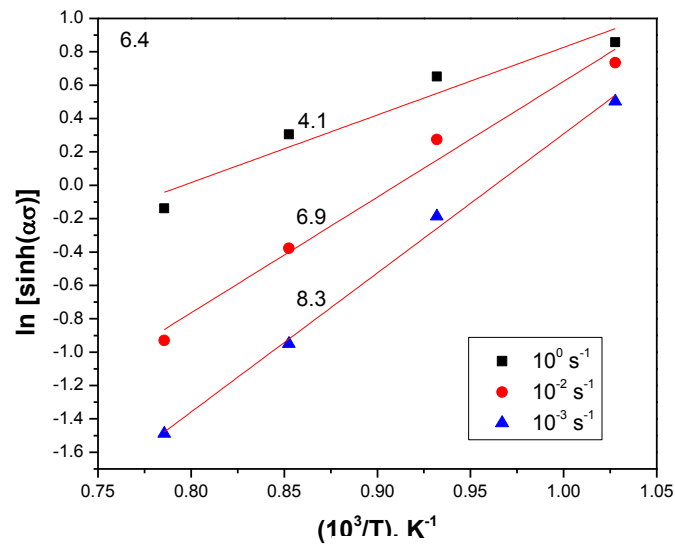


b

Fig.4.2: Determination of (a) n and (b) β at a constant strain $\epsilon = 0.6$.



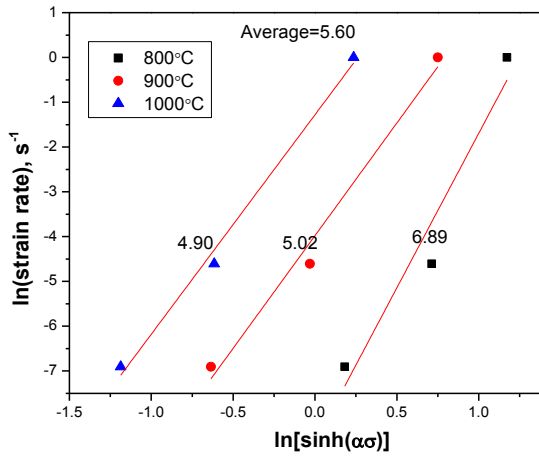
a



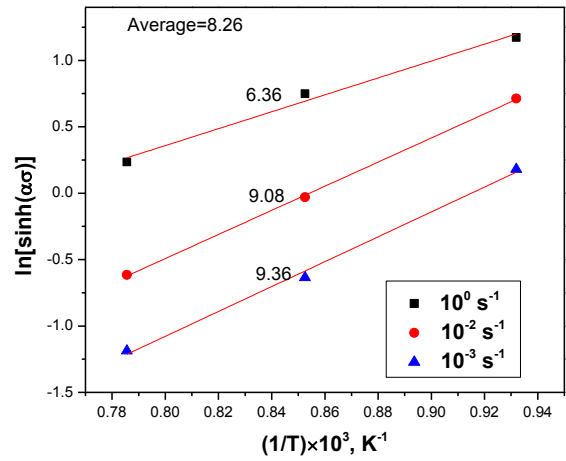
b

Fig.4.3: The plot of (a) $\ln \dot{\epsilon}$ vs $\ln [\sinh \alpha\sigma]$ and (b) $\ln [\sinh \alpha\sigma]$ vs $1/T$ (at a constant strain $\epsilon = 0.6$) for the determination of (a) n and (b) activation energy.

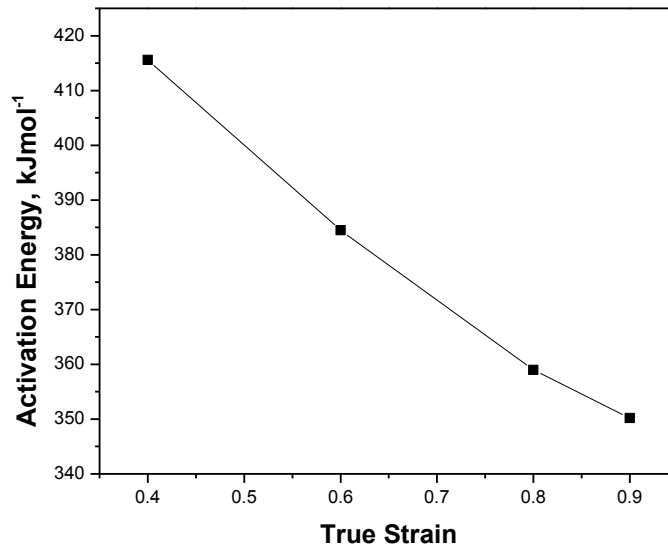
It may be noted that fitting of the data for 700°C/1 condition is particularly different than other conditions. The flow curve for 700°C/1 appears distinctly different. The curve shows a typical strain hardening behavior up to a strain of $\epsilon=0.5$ and does not extend up to $\epsilon=0.9$ unlike other flow curves. This may particularly affect the fitting of the data leading to abnormally high value of n . The exclusion of the data will evidently result in the elimination of other deformation conditions at 700°C (since a perfect fit can be obtained for two data points). Therefore, the plots are recalculated excluding the 700°C condition. The calculated n value excluding the 700°C data is 7.5. Similarly, the value of β excluding the 700°C data is 0.036. The value of α ($=\beta/n$) is 0.0047. The modified Q can be calculated from the equation Eq. 4.10. Fig.4.4(a) and Fig.4.4(b) shows the $\ln \dot{\epsilon}$ vs $\ln[\sinh(\alpha\sigma)]$ and $\ln[\sinh \alpha\sigma]$ vs $1/T$ plots, respectively sans the 700°C data at the strain value of $\epsilon=0.6$. The n values at 800°C, 900°C and 1000°C are found to be ~4.90, 5.02 and 6.89, respectively (Fig.4.4(a)). On the other hand, the average value of the slope obtained from the $\ln[\sinh \alpha\sigma]$ vs $1/T$ plot is 8.26 (Fig.4.4(b)). The product of these two quantities gives the activation energy at the specified strain level. In a similar manner, the activation energy is calculated at other strain levels. The variation of activation energy with temperature is shown in Fig.4.4(c). The activation energy decreases with increasing strain. A particularly high value is observed for $\epsilon=0.4$ (415 kJmol⁻¹). For $\epsilon>0.4$, the activation energy drops from 375 kJmol⁻¹ to 350 kJmol⁻¹.



(a)



(b)



(c)

Fig.4.4: The plot of (a) $\ln \dot{\epsilon}$ vs $\ln [\sinh \alpha\sigma]$ and (b) $\ln [\sinh \alpha\sigma]$ vs $1/T$ (at a constant strain $\epsilon = 0.6$) for the determination of (a) n and (b) activation energy sans the 700°C data; (c) shows the variation of activation energy with imposed strain.

The interdependence of temperature and strain rate can be shown in a single parameter Z , which was proposed by Zener and Hollomon can be given as

$$Z = \dot{\epsilon} \exp\left(\frac{Q}{RT}\right) \quad \text{Eq.(4.8)}$$

Upon, comparing with eq.(4.1), eq.(4.8) can also be written as

$$Z = \dot{\epsilon} \exp\left(\frac{Q}{RT}\right) = A[\sinh(\alpha\sigma)]^n \quad \text{Eq.(4.9)}$$

Taking log function on both sides, eq.(4.9) results in,

$$\ln Z = \ln A + n \ln[\sinh(\alpha\sigma)] \quad \text{Eq.(4.10)}$$

The linear fit with $\ln Z$ versus $\ln [\sinh(\alpha\sigma)]$, gives the slope as 'n' and y-intercept as $\ln A$, this is shown in Fig.4.5.

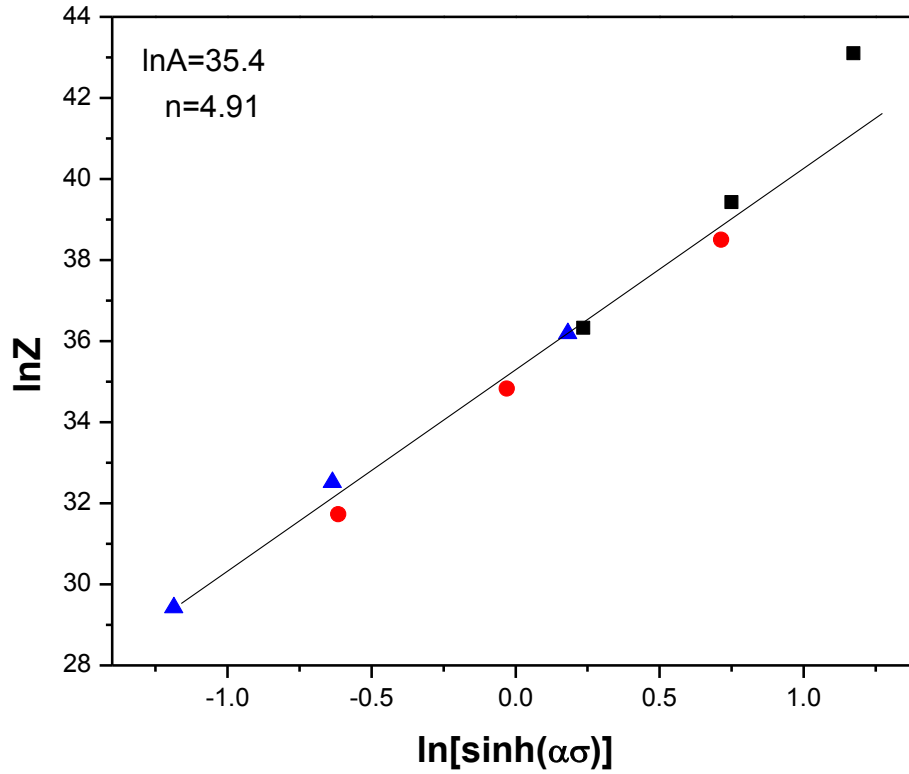


Fig.4.5: The linear dependence of Z on hyperbolic sine function of flow stress at $\epsilon=0.6$.

Based on the above analysis, a constitutive equation eq.(4.1) can be developed which describes the flow stress as a function of temperature and strain rate at $\epsilon=0.6$ as,

$$\dot{\epsilon} = 2.36 \times 10^{15} [\sinh(0.0047\sigma)]^{4.91} \exp\left(\frac{-384500}{8.314 \times T}\right)$$

4.4 Evolution of microstructure and texture

The evolution of microstructure during hot deformation under different processing conditions is shown in Fig.4.6. The microstructures shown in Fig.4.6 are basically the image quality (IQ) maps overlaid with grain boundaries (GBs). The low angle grain boundaries (LAGBs defined by $2^\circ \leq \text{misorientation angle } (\theta) \leq 15^\circ$) and high angle grain boundaries (HAGBs defined by $\theta \geq 15^\circ$) are shown by red and blue lines, respectively. The contrast visible in the IQ maps are based on contrast of the acquired kikuchi diffraction patterns. The IQ maps, therefore, correlate with the defect density. It may be noticed that the maps in Fig.4.5 has been arranged in the decreasing

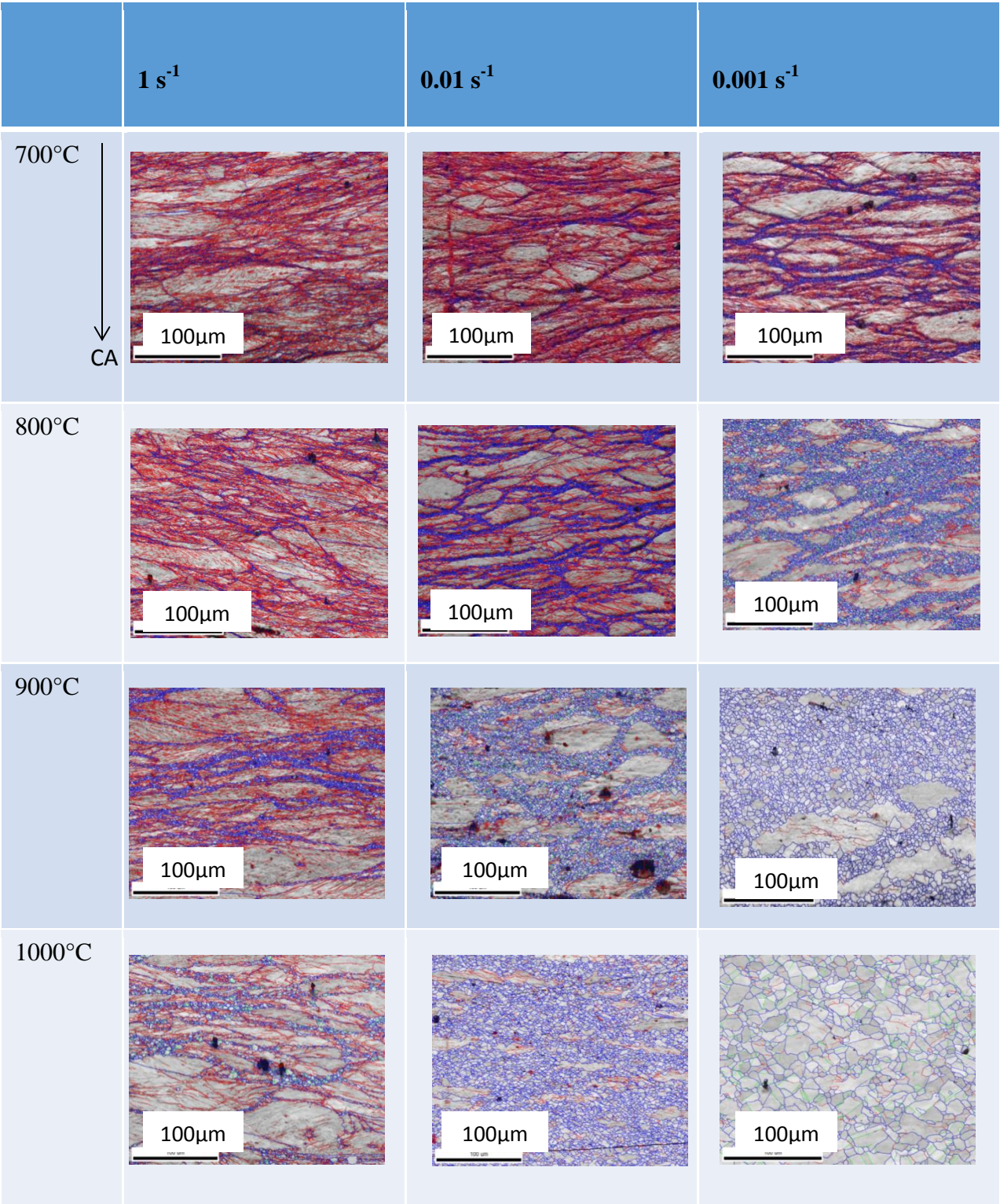


Fig.4.6. Image Quality + Grain Boundary Maps showing the evolution of Microstructure during deformation at various deformation parameters.

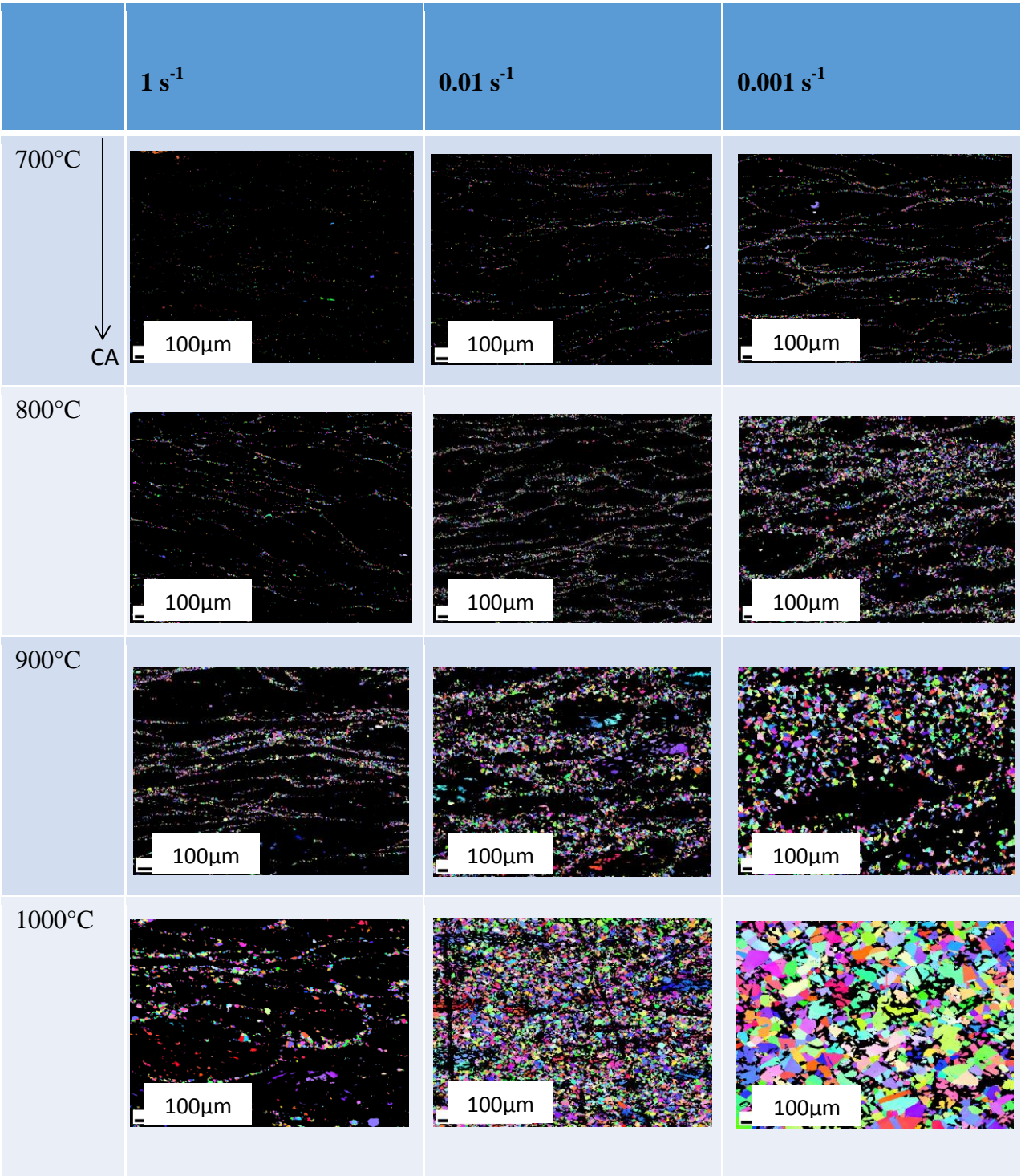


Fig.4.7. IPF Maps for the DRX regions during deformation at various conditions.

order of the Zener-Hollomon parameter ($z = \dot{\epsilon} \exp(\frac{Q}{kT})$) along the vertical direction and along the horizontal direction. This is also clearly indicated in the figure.

The main observations from the IQ maps can now be summarized. It may be very clearly observed that the volume fraction of the DRX grains increase systematically with decreasing Z i.e. for constant temperature with decreasing strain rate or for constant strain rate with increasing temperature. The IQ maps of materials deformed at 700°C and higher strain rates show rather small fraction of DRX (for strain rates of 1 and 0.1, corresponding to Fig.4.5(a) and Fig.4.5(b), respectively). Formation of profuse micro shear bands and their propagation is a remarkable feature. Sometimes the shear bands converge into the GBs and split the microstructure remarkably. The width of the bands may go up to 30 μm . Remarkably, these small fraction of DRX grains are observed to nucleate preferentially along the micro shear bands which sometimes coincide with the grain boundaries. For processing condition 700°C/0.001 (Fig.4.6(c)), DRX is clearly evidenced by nucleation of ultrafine grains (average grain size $\sim 0.80\mu\text{m}$) at the shear bands and at the prior grain boundaries. These DRX grains are bounded by HAGBs so that their nucleation is accompanied with high concentration of HAGBs at the prior GBs and shear bands. On the other hand, at deformation temperature of 1000°C and for various strain rates, high fraction of DRX grains are observed in all the IQ maps (Fig.4.6(j)-Fig.4.6(l)). Almost completely DRXed microstructure is obtained at the processing condition of 1000°C/0.001 (Fig.4.6(l)). The DRXed grains in this condition (Fig.4.6(l)) also show presence of clear annealing twin boundaries (highlighted by the green lines). The microstructures at other combination of temperature/strain rate show varying fraction of DRXed grains. It may be noticed that at higher temperatures and lower strain rates (for lower Z) prior grain boundaries emerge as the preferred nucleation sites for dynamic recrystallization. In order to further understand the microstructural development, the DRXed fraction is separated from the IQ maps. The corresponding maps are shown in Fig.4.7 in the form of IPF maps. The reference direction in the IPF maps is the CA. The DRX grain size is estimated from these maps while the DRX fraction is directly obtained from the fraction of points which belong to the portioned dataset. Table 4.1 summarizes the grain size and DRX fraction for different processing conditions, quantitatively. It is clearly observed that DRXed grain size and fraction DRXed decreases with increasing Z . In order to understand the texture evolution during hot compression, the CA-IPFs are calculated from the deformed (Fig.4.8) and recrystallized (Fig.4.9) fractions. It is clearly observed from the

IPF maps that the texture of both deformed and recrystallized regions are quite weak. In case of deformed regions weak alignment of the CA parallel to the $\langle 100 \rangle$ or $\langle 111 \rangle$ pole is observed. It is clearly observed from the IPF maps that the dynamically recrystallized grains show rather random and scattered orientations (Fig.4.7). In good agreement the IPF plots show very weak intensities (Fig.4.9). In most cases the ODF intensity is close to the random level (~ 1). Rather weak alignment of the CA parallel to the $\langle 100 \rangle$ or $\langle 111 \rangle$ pole is observed.

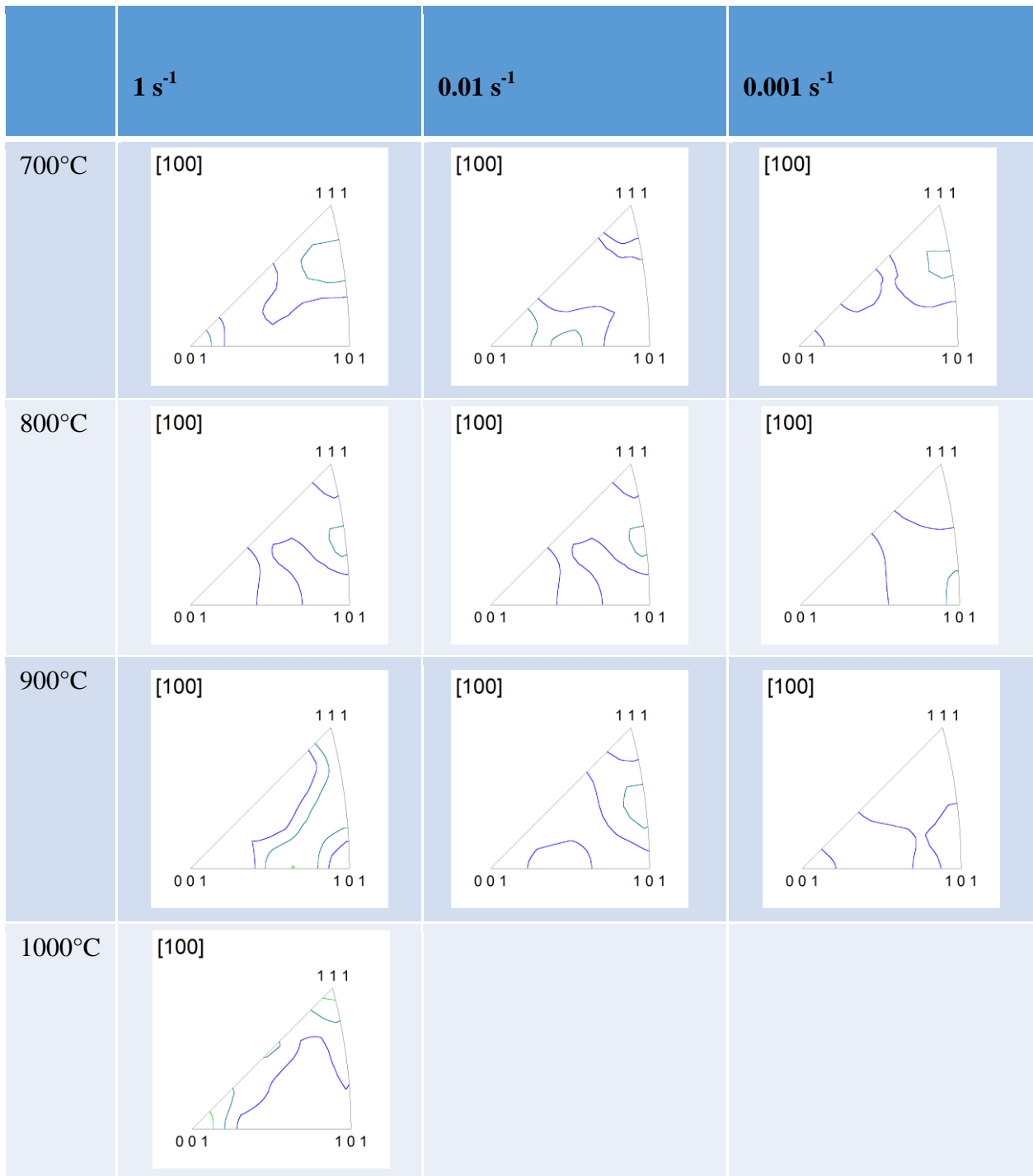


Fig.4.8. IPF plots showing the crystallographic poles in the deformed regions that are oriented parallel to the compression axis.

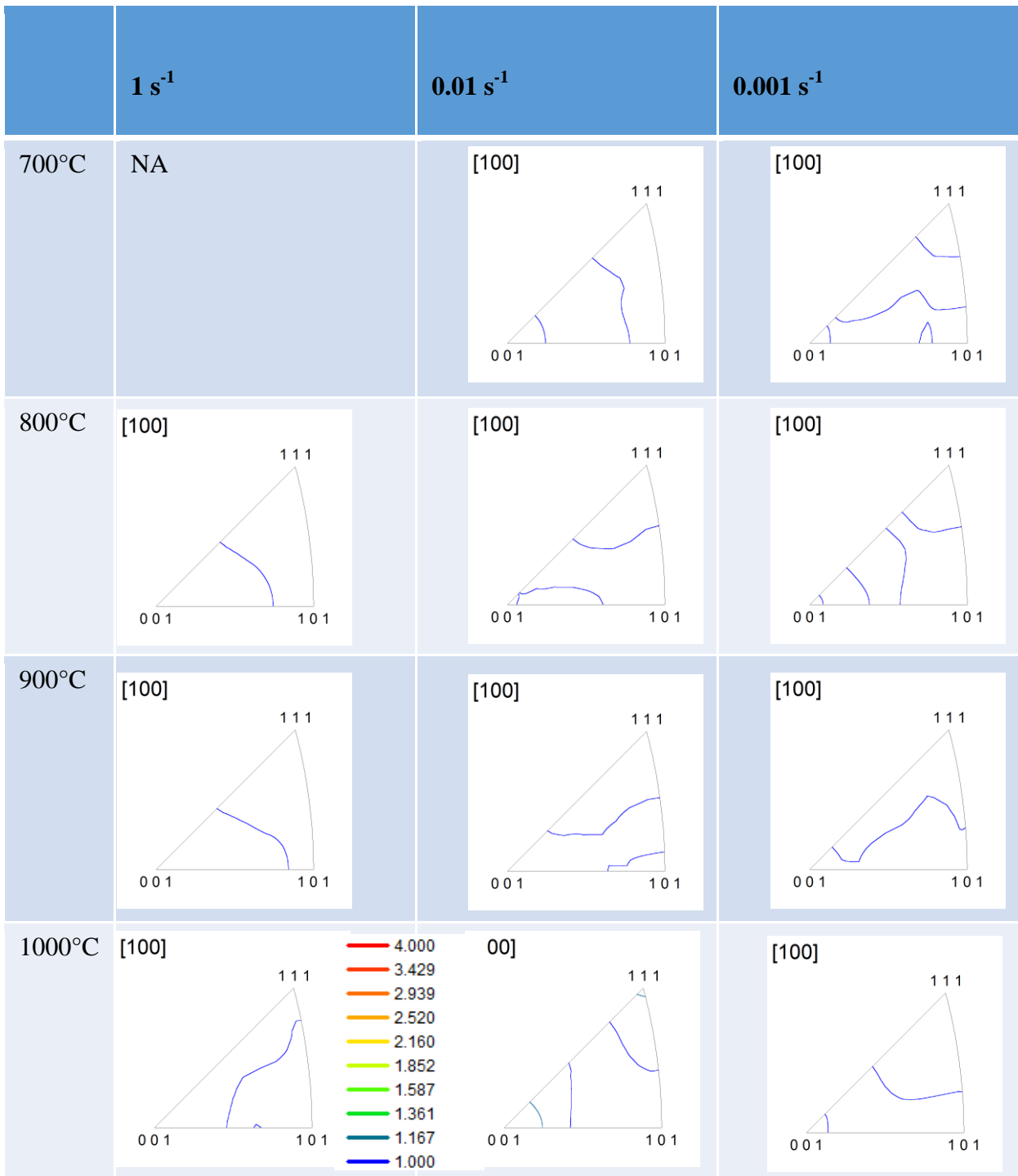




Fig.4.9. IPF plots showing the crystallographic poles in the DRX regions that are oriented parallel to the compression axis.

Table.4.1. Summary of DRX fraction and DRX grain size at various deformation conditions.

Temperature (°C) 	DRX fraction (%)			DRX grain size(μm)		
	Strain rate, s⁻¹ 	10 ⁰	10 ⁻²	10 ⁻³	10 ⁰	10 ⁻²
700	0.8	2.3	6	-	0.80	0.87
800	3	8.1	18.5	0.7	0.87	1.2
900	8	23	27	1.04	1.5	2.58
1000	9	48	73	1.32	1.57	5

5. Discussion

5.1 Flow curve and hot deformation behavior

The flow curve analysis shows that the activation energy in the steady state varies from ~ 380 kJ mol^{-1} to 350 kJ mol^{-1} . This activation energy is somewhat higher than that reported by Stepanov et al [29] ~ 291 kJ mol^{-1} . These authors have shown reasonable correlation of this activation energy with that of the slowest moving diffusion species i.e. Ni ~ 317.5 kJ mol^{-1} . On the other hand, the activation energy during tensile testing of the same alloy during tensile testing at temperatures $\geq 750^\circ\text{C}$ and at a strain rate of 10^{-5} s^{-1} is found to be ~ 330 kJ mol^{-1} . This activation energy is clearly in good agreement with the lower bound value of the activation energy in the present research ~ 350 kJ mol^{-1} . This apparent similarities indicate similar diffusion controlled mechanism for hot deformation in the present system. The apparent differences in the activation energy with that reported by Stepanov et al [29] may also originate from the initial microstructure. In the present case the microstructure before hot compression is wrought processed with relatively fine microstructure ~ 28 μm . The initial microstructure has not been reported by Stepanov et al [29].

5.2 Evolution of microstructure and texture

The recrystallization behavior during hot compression can be categorized in two broad classes depending up on the nucleation mechanism, namely continuous and discontinuous dynamic recrystallization (CDRX and DDRX, respectively) [30]. In case of CDRX, the evolution of a recrystallized microstructure connected by HAGB network is through the process of conversion of LAGBs to HAGBs with increasing strain. In contrast, the DDRX mechanism involve nucleation and growth of new strain free grains. The IQ maps shown in Fig.4.5 clearly reveal the process of DDRX during hot compression. Even in case of the $700^\circ\text{C}/1$ (Fig.4.6(a)) and $700^\circ\text{C}/0.01$ (Fig.4.6(b)) deformation conditions, nucleation of grains at the shear bands are evidenced although the DRX fraction is rather small in these conditions. In general shear bands are regions of large orientation gradient which is favorable for easy nucleation during static or dynamic recrystallization. In contrast, conditions which involve high temperature and low strain rates GBs are preferential sites for nucleation. This may be expected due to the fact that higher temperature and low strain rate decreases the propensity for shear band formation and also reduce the volume of material involved in shear deformation. It may be noted that the flow

curves at 700°C/1 and 700°C/0.01 shows visible serrations which indicates the propensity for extensive shear band formation. The process of DDRX in the present system has also been confirmed over a wide temperature range by Stepanov et al [29]. Extensive bulging of the initial grain boundaries could be observed at the initial stages in the process of formation of the recrystallization nuclei. The mechanism suggested by Stepanov et al [29] could not be confirmed in the present work due to the unavailability of very high resolution maps. The uniaxial compression texture of medium to low SFE materials are described by the development of CA//<110> fiber texture. However, in the present HEA the compression texture appears significantly different. The main characteristics are presence of very elongated deformed grains having orientations CA//<001> or CA//<111> axis along with few grains having the typical CA//<110> orientation. As a result, the deformed regions in the HEA shows weak and diffuse texture. The DRXed grains show rather weak and diffuse texture. In case of nucleation at shear bands this is consistent with the fact that shear bands contain random orientations with large orientation spread [27]. Therefore, nucleation and growth of the grains from the shear bands at the expense of the deformed matrix should result in the development of a very weak texture. However, even in case of grain boundary nucleation, the texture is found to be very weak. In the present case the weak compression texture also contributes to weak and diffuse texture after complete recrystallization. This behavior is found to be quite consistent with texture weakening as many grains rotate out from the compression texture components during DRX [30]. In the present case if nucleation happens along the grain boundaries without any preferential orientation selection features of the deformed regions should be reproduced. Since the deformed regions show very weak <100> and <111> fibers, this is also displayed by the DRX fraction.

Chapter 6: Summary and conclusions

The hot deformation behaviour of equiatomic CoCrFeMnNi is studied in the present work. The following major conclusions may be drawn from the present study:

- (i) The flow curve at temperatures $\geq 800^{\circ}\text{C}$ shows dynamic recrystallization behaviour.
- (ii) The difference between peak stress and steady state stress is not found to be significant.
- (iii) The activation energy varies from 350 kJ mol^{-1} to 375 kJ mol^{-1} at strain levels ranging from $\varepsilon=0.5$ to $\varepsilon=0.9$.
- (iv) The dynamically recrystallized microstructure shows evidence of nucleation at shear bands and at the grain boundaries.
- (v) Significant grain refinement is achieved due to dynamic recrystallization. In the case of $1000^{\circ}\text{C}/0.001$ condition, the average grain size is $\sim 5 \mu\text{m}$ which indicates significant grain refinement as compared to the starting material with average grain size $\sim 28 \mu\text{m}$.
- (vi) The texture of dynamically recrystallized materials are found to be generally weak. The deformed regions show rather weak $\langle 001 \rangle$ and $\langle 111 \rangle$ fiber and very similar texture is observed in the dynamically recrystallized regions.
- (vii) The evolution of texture in the alloy indicates nucleation of dynamically recrystallized grains without any preferential orientation selection.

References

1. Yeh, J.W., et al., *Nanostructured high-entropy alloys with multiple principal elements: Novel alloy design concepts and outcomes*. *Advanced Engineering Materials*, 2004. **6**(5): p. 299-303.
2. Yeh, J.W., et al., *Formation of simple crystal structures in Cu-Co-Ni-Cr-Al-Fe-Ti-V alloys with multiprincipal metallic elements*. *Metallurgical and Materials Transactions A: Physical Metallurgy and Materials Science*, 2004. **35 A**(8): p. 2533-2536.
3. Zhang, Y., et al., *Microstructures and properties of high-entropy alloys*. *Progress in Materials Science*, 2014. **61**(0): p. 1-93.
4. Yeh, J.W., *Alloy Design Strategies and Future Trends in High-Entropy Alloys*. *Jom*, 2013. **65**(12): p. 1759-1771.
5. Gludovatz, B., et al., *A fracture-resistant high-entropy alloy for cryogenic applications*. *Science*, 2014(6201): p. 1153-1158.
6. Zhang, Y., et al., *High-entropy alloys with high saturation magnetization, electrical resistivity, and malleability*. *Scientific Reports*, 2013. **3**.
7. Tsai, M.-H. and J.-W. Yeh, *High-Entropy Alloys: A Critical Review*. *Materials Research Letters*, 2014. **2**(3): p. 107-123.
8. Miracle, D.B., et al., *Exploration and Development of High Entropy Alloys for Structural Applications*. *Entropy*, 2014. **16**(1): p. 494-525.
9. Lu, Y., et al., *A Promising New Class of High-Temperature Alloys: Eutectic High-Entropy Alloys*. *Scientific Reports*, 2014. **4**: p. 6200.
10. Tsai, K.Y., M.H. Tsai, and J.W. Yeh, *Sluggish diffusion in Co–Cr–Fe–Mn–Ni high-entropy alloys*. *Acta Materialia*, 2013. **61**(13): p. 4887-4897.
11. Otto, F., et al., *The influences of temperature and microstructure on the tensile properties of a CoCrFeMnNi high-entropy alloy*. *Acta Materialia*, 2013. **61**(15): p. 5743-5755.
12. Chuang, M.H., et al., *Microstructure and wear behavior of Al_xCo_{1.5}CrFeNi_{1.5}Ti_y high-entropy alloys*. *Acta Materialia*. **59**(16): p. 6308-6317.
13. Hughes, D.A. and N. Hansen, *High angle boundaries formed by grain subdivision mechanisms*. *Acta Materialia*, 1997. **45**(9): p. 3871-3886.
14. Valiev, R.Z. and T.G. Langdon, *Principles of equal-channel angular pressing as a processing tool for grain refinement*. *Progress in Materials Science*, 2006. **51**(7): p. 881-981.
15. Zhilyaev, A.P. and T.G. Langdon, *Using high-pressure torsion for metal processing: Fundamentals and applications*. *Progress in Materials Science*, 2008. **53**(6): p. 893-979.
16. Tsuji, N., et al., *ARB (Accumulative Roll-Bonding) and other new Techniques to Produce Bulk Ultrafine Grained Materials*. *Advanced Engineering Materials*, 2003. **5**(5): p. 338-344.
17. Bhattacharjee, P.P., et al., *Microstructure and texture evolution during annealing of equiatomic CoCrFeMnNi high-entropy alloy*. *Journal of Alloys and Compounds*, 2014. **587**: p. 544-552.
18. Otto, F., N.L. Hanold, and E.P. George, *Microstructural evolution after thermomechanical processing in an equiatomic, single-phase CoCrFeMnNi high-entropy alloy with special focus on twin boundaries*. *Intermetallics*, 2014. **54**: p. 39-48.
19. Shaysultanov, D.G., et al., *Phase composition and superplastic behavior of a wrought AlCoCrCuFeNi high-entropy alloy*. *JOM*, 2013. **65**(12): p. 1815-1828.
20. Kuznetsov, A.V., et al., *Tensile properties of an AlCrCuNiFeCo high-entropy alloy in as-cast and wrought conditions*. *Materials Science and Engineering A*, 2012. **533**: p. 107-118.
21. Tsai, C.W., et al., *Effect of temperature on mechanical properties of Al_{0.5}CoCrCuFeNi wrought alloy*. *Journal of Alloys and Compounds*, 2010. **490**(1-2): p. 160-165.

22. Park, N., et al., *Recrystallization Behavior of CoCrCuFeNi High-Entropy Alloy*. Metallurgical and Materials Transactions A: Physical Metallurgy and Materials Science, 2015. **46**(4): p. 1481-1487.
23. Bhattacharjee, P.P., et al., *Microstructure and texture evolution during annealing of equiatomic CoCrFeMnNi high-entropy alloy*. Journal of Alloys and Compounds, 2014. **587**(0): p. 544-552.
24. Sathiaraj, G.D. and P.P. Bhattacharjee, *Analysis of microstructure and microtexture during grain growth in low stacking fault energy equiatomic CoCrFeMnNi high entropy and Ni-60wt.%Co alloys*. Journal of Alloys and Compounds, 2015. **637**: p. 267-276.
25. Liu, W.H., et al., *Grain growth and the Hall-Petch relationship in a high-entropy FeCrNiCoMn alloy*. Scripta Materialia, 2013. **68**(7): p. 526-529.
26. Nayan, N., et al., *Hot deformation behaviour and microstructure control in AlCrCuNiFeCo high entropy alloy*. Intermetallics, 2014. **55**(0): p. 145-153.
27. Humphreys, F.J. and M. Hatherly, in *Recrystallization and Related Annealing Phenomena (Second Edition)*. 2004, Elsevier: Oxford.
28. Grotheer, H.H., et al., *Elementary Reactions in the Methanol Oxidation System .1. Establishment of the Mechanism and Modeling of Laminar Burning Velocities*. Berichte Der Bunsen-Gesellschaft-Physical Chemistry Chemical Physics, 1992. **96**(10): p. 1360-1376.
29. Stepanov, N.D., et al., *High temperature deformation behavior and dynamic recrystallization in CoCrFeNiMn high entropy alloy*. Materials Science and Engineering: A, 2015. **636**(0): p. 188-195.
30. Sakai, T., et al., *Dynamic and post-dynamic recrystallization under hot, cold and severe plastic deformation conditions*. Progress in Materials Science, 2014. **60**(0): p. 130-207.